PCCP

PAPER

View Article Online
View Journal | View Issue

Open Access Article. Published on 28 lokakuuta 2025. Downloaded on 26.3.2026 20.36.49.
This article is licensed under a Creative Commons Attribution-NonCommercial 3.0 Unported Licence.

Check for updates

Cite this: *Phys. Chem. Chem. Phys.*, 2025, **27**, 24589

# Kinetic modeling of ammonia and hydrogen dissociative co-adsorption on iron surface and its effect on hydrogen embrittlement

Nan Zhang,*[ac] Kentaro Wada,[a] Ryuoske Komoda,[b] Aleksandar Staykov[a] and Masanobu Kubota*[a]

Received 25th June 2025,
Accepted 28th October 2025

DOI: 10.1039/d5cp02423d

rsc.li/pccp

We study the mitigation of environmental hydrogen embrittlement of iron by ammonia impurities in the hydrogen gas using combined theoretical and experimental methods. The competitive and dissociative co-adsorption of gaseous ammonia and gaseous hydrogen on the iron surface was investigated using density functional theory. The surface adsorption and decomposition of ammonia, as well as the ammonia partial pressure, were considered as influential factors contributing to the control of atomistic hydrogen uptake into the material. To elucidate the mechanism of ammonia competing with hydrogen on the iron surface and of ammonia mitigating hydrogen embrittlement, we develop kinetic modeling that can estimate the reaction rate and the dynamic surface coverage of different adsorbed species on the iron surface. The reaction rates for hydrogen and ammonia co-adsorption and dissociation were calculated using transition state theory combined with the Langmuir adsorption model, and a fracture toughness test was conducted to validate theoretical results. The adsorption rate of ammonia on iron is significantly higher compared to hydrogen, thus, ammonia hinders the hydrogen adsorption on the iron surface. However, partial pressure dependent ammonia decomposition also provides hydrogen atoms, which induce hydrogen embrittlement. The theoretical results of this study were supported well by experimental fracture toughness test results.

## 1. Introduction

The combination of environmental and economic factors led to the wider adoption of hydrogen as an energy source and energy storage compound. The abundance of renewable energy sources combined with steam electrolyzes could successfully convert renewable energy into chemical fuel ($H_2$) that can be stored and transported over long distances. Hydrogen can be utilized in the chemical industry, in fuel cells for stationary and mobile generation of electricity, and in combustion turbines on its own or in mixtures with hydrocarbons. However, hydrogen causes degradation of material strength of metal components such as storage containers and pipelines, which is generally known as hydrogen embrittlement (HE) of metals. HE is caused by the diffusion of hydrogen atoms into the metal lattice, leading to the formation of brittle hydride phases,[1] weakening of metal bonds,[2] enhancement of localized plasticity,[3] and so on resulting in lower resistance to fracture, which can cause sudden and catastrophic failure. HE manifests as ductility loss in the tensile tests, fatigue crack growth acceleration, and fracture toughness reduction.[4–8] In the gaseous hydrogen environment, hydrogen uptake from the environment into the material is the first step for HE of iron (Fe) and steel. In the process of hydrogen uptake at room temperature, the dissociation of hydrogen molecules into hydrogen atoms is assisted by catalysis of the iron surface.[9] In this context, if the catalysis of the Fe surface is suppressed by surface catalytic poisons the HE could be significantly delayed.[10–16] The strategy of adding ppm level gaseous impurities to the hydrogen gas to mitigate the HE is attracting more attention because the impurity mitigation strategy allows us to use the existing steel pipelines and storage vessels utilized for natural gas without the construction of expensive, hydrogen resistant infrastructure. For instance, the well-established natural gas pipeline could be employed for hydrogen gas transportation. The impurity mitigation strategy has the potential to accelerate the adoption of hydrogen energy at reduced cost. Nagao *et al.* experimentally demonstrated that exposure of the SCM435 low-alloy steel, whose surface is covered by a natural oxide layer, to 120 MPa $H_2$ gas at room

[a] *International Institute for Carbon Neutral Research, Kyushu University, Fukuoka, Japan*
[b] *Department of Mechanical and Control Engineering, Kyushu Institute of Technology, Kitakyushu, Japan*
[c] *Department of Mechanical Engineering, Nagaoka University of Technology, Nagaoka, Japan. E-mail: nanzhang@vos.nagaokaut.ac.jp*

Open Access Article. Published on 28 lokakuuta 2025. Downloaded on 26.3.2026 20.36.49.
This article is licensed under a Creative Commons Attribution-NonCommercial 3.0 Unported Licence.

temperature caused no increase in the hydrogen concentration in the material.[17] It implies that hydrogen uptake from $H_2$ gas into the steel at room temperature requires fresh iron surface, which can act as a catalytic site for the dissociation of molecular hydrogen into atomic hydrogen. Fresh iron surface is created by crack propagation initially through the native oxide layer.[18] Staykov *et al.* explained the role of the iron surface as a catalyst for the dissociation of $H_2$ molecules by density functional theory (DFT) calculations and elucidated the mechanism of $O_2$ mitigation effect on HE.[19] The iron surface should be clean in order to act as a catalyst for the $H_2$ dissociation. Preadsorbed oxygen on the iron surface hinders the catalytic activity by localization of the electron density. Somerday *et al.* considered that the hydrogen uptake from hydrogen gas occurs at the newly created surfaces during crack propagation. They experimentally confirmed both the hydrogen uptake through the surfaces created during crack propagation and the blocking of hydrogen uptake by preadsorbed oxygen based on their crack propagation tests of X52 steel.[20]

In addition to oxygen, carbon monoxide (CO) is well-studied as a mitigator of HE.[21,22] Komoda *et al.* clarified the mitigation effects of CO and $O_2$ on the HE is focusing on their adsorption rates on the iron surface. Staykov *et al.* theoretically calculated the ratio of the impurity-occupied sites to free sites on the surface in order to interpret the result of the fracture toughness tests.[21] They showed that $O_2$ coverage is 100%, while that of CO is less than 75%.[21,22] These results are useful for understanding the different HE mitigation properties of $O_2$ and CO impurities. While both $O_2$ and CO show excellent HE mitigation effects, there are some limitations to their industrial applications. For example, $O_2$ forms explosive mixtures with $H_2$ at higher concentrations, thus mixing $O_2$ and $H_2$ is considered a safety issue.[23] CO is a catalytic poison for platinum nanoparticles in polymer electrolyte fuel cell and is an undesired impurity for industrial applications.[24] CO mitigation effect is also limited to low pressure and short time intervals owing to the incomplete surface coverage. Thus, the mitigation effects of these impurities should be utilized in their respective suitable contexts. Therefore, to industrially use the mitigation effects of impurities more broadly, it is necessary to comprehensively elucidate the influences of other impurities besides $O_2$ and CO.

In this context, we focused on ammonia ($NH_3$) because it does not imply industrial safety issues and does not have a poisoning effect on the catalytic activity of platinum. However, the number of studies on the effect of $NH_3$ on HE is very limited. Srikrishnan *et al.* reported that $NH_3$ mitigated hydrogen-assisted crack growth of iron.[25] They carried out the crack growth experiment of 4340 steel under $H_2$ gas and $H_2$ gas mixed with 50 ppm in volume (vppm) $NH_3$ at 330 Pa of gas pressure, the result showed that the 50 vppm $NH_3$ significantly reduced the crack growth speed compared with that in the pure $H_2$. On the other hand, $NH_3$ induces stress corrosion cracking, which is one of the forms of hydrogen embrittlement.[26] Also, degradation of the tensile strength properties is induced in the $NH_3$ environment.[27] Thus, the effect of $NH_3$ on HE is complicated as it can both mitigate and induce HE. The mitigation mechanism of $NH_3$ on HE remains unclear.

In addition to first-principles energetics, a kinetic framework is needed to translate elementary adsorption and dissociation steps into observable surface coverages and rates under realistic gas compositions. A mean-field (Langmuir-type) microkinetic treatment provides this bridge by mapping DFT-derived barriers and adsorption energies to competitive and dissociative co-adsorption of $NH_3$ and $H_2$, thereby rationalizing how partial pressures and temperature control the instantaneous availability of catalytic sites and the net hydrogen supply to iron. Such models are widely used as a pragmatic baseline for trend-level comparisons and for screening mitigation strategies, especially when experiments alone cannot resolve fast interfacial steps. Here we adopt this framework to quantify $NH_3$–$H_2$ competition on Fe(110) and to connect surface reaction kinetics to hydrogen-embrittlement outcomes. The bcc Fe(110) facet is the thermodynamically most stable (lowest surface free energy) over the stability range of bcc iron, and thus a commonly exposed and extensively studied model surface. It is routinely prepared and characterized as a clean single-crystal surface in UHV studies.

In this work, we use first-principle methods to investigate the co-adsorption of $NH_3$ and $H_2$ on the iron Fe(110) surface, including $NH_3$ molecular adsorption, $NH_3$ decomposition, and its competition with $H_2$ dissociation. We investigated the $NH_3$ adsorption rate and decomposition rate based on the transition state theory. Furthermore, we investigate the effect of preadsorbed $NH_3$ on the $H_2$ dissociation. Those processes are significant factors that control the $NH_3$ and H coverage on iron surface. We established a kinetic model to calculate the coverage of $NH_3$, $NH_3$-derived species, and $H_2$-derived H atoms on the Fe surface and investigated the $NH_3$ partial pressure effect on the $NH_3$-derived H atom coverage. In addition, we performed a fracture toughness test of JIS SCM440 Cr–Mo steel in $H_2$, $NH_3$ and $H_2$ mixture, $NH_3$ and $N_2$ mixture, and $N_2$ gases under gas pressure were 0.1 MPa in order to validate the calculation results. This material suffered from hydrogen embrittlement.

## 2. Methods of investigation

### 2.1 Theory

Periodic DFT was performed using Numerical Atomic Orbitals (NAO) implemented in Quantum ATK.[28] The method is based on quantum mechanics principles and can be used to investigate the structural and electronic properties of materials.[29] The GGA Perdew–Burke–Ernzerhof (PBE) exchange–correlation functional was applied using Fritz-Haber-Institute (FHI) pseudopotentials. Electron energies were converged to $10^{-6}$ eV using double zeta polarized (DZP) basis set for all valence electrons. All calculations were spin polarized. The calculations were performed with Monkhorst–Pack *k*-point mesh of $8 \times 8 \times 8$ (properly describe the properties of one unit cell for the BCC bulk iron lattice) and $4 \times 4 \times 1$ for the Fe(110) terminated iron

 This journal is © the Owner Societies 2025

Open Access Article. Published on 28 lokakuuta 2025. Downloaded on 26.3.2026 20.36.49.
This article is licensed under a Creative Commons Attribution-NonCommercial 3.0 Unported Licence.

slab. The geometry relaxation was performed until the forces converged to values below 0.05 eV Å$^{-1}$. For bulk systems, relaxation was performed for the cell volume, cell shape, and atomic positions. For slab models, relaxation was performed for the atomic positions only. Slabs were constructed using 6 alternating iron layers. The coordinates of the atoms in the middle two layers were fixed, while the coordinates of the top two and bottom two were fully relaxed. Activation barriers for various reaction mechanisms were obtained using the climbing image-nudged elastic band method (CI-NEB). In the process of NEB calculations, eight to ten images were used between the starting and the ending geometries of reactions. Adsorption energies and activation barriers are reported as 0 K DFT total energies without free-energy corrections. This pragmatic approximation is widely used in surface reaction studies[30] (Exploring $CO_2$ hydrogenation to methanol at a CuZn–$ZrO_2$ interface *via* DFT calculations). These assumptions may not strictly hold for $NH_3$/H co-adsorption on Fe(110); however, within the coverage range examined (11–33%), this approximation is widely used and adequate for trend-level comparisons. Moreover, dissociative $H_2$ adsorption is treated with the standard $\sqrt{p(H_2)}$ dependence to reflect its two-site requirement. Coverage-dependent DFT energetics (Tables 3 and 5) partially account for lateral interactions by parameterizing rate/equilibrium constants at explicit coverages. Potential refinements (*e.g.*, Fowler–Guggenheim/Temkin isotherm) are discussed in the SI-S1.

In this study, the vibrational frequencies of normal modes of the decomposition reaction of $NH_3$ and dissociation reaction of $H_2$ were calculated by combining the dynamical matrix and vibrational mode calculation of Quantum ATK. Initial and transition geometry were converged to $10^{-8}$ eV to ensure that the vibrational frequency calculation yields proper results because vibrational frequency calculation requires well-converged electron density. Each ion in the cell is then displaced by ±0.01 Å in all directions of the cartesian vector, then a Hessian matrix was constructed from the force which shows how atoms react to displacement. Force derivative tolerance is set to $10^{-3}$ eV Å$^{-1}$. Once the normal mode vibrational frequencies of the system were obtained, all data was (excluding the imaginary vibration of the transition state) divided by the product of the data from the initial geometry to obtain the attempt frequency.

$$A = \frac{\prod_{i=1}^{3N} v_i^{O}}{\prod_{i=1}^{3N} v_i^{S}} \tag{1}$$

where $\prod_{i=1}^{3N} v_i^{O}$ is multiplying all vibrational frequency at initial configuration, $\prod_{i=1}^{3N} v_i^{S}$ is multiplying all vibrational frequency at transition state configuration (has one more imaginary frequency).

Table 1 Chemical composition of SCM440 (mass%)

| Fe | C | Si | Mn | P | S | Cu | Ni | Cr | Mo |
|---|---|---|---|---|---|---|---|---|---|
| Bal. | 0.40 | 0.22 | 0.63 | 0.008 | 0.004 | 0.02 | 0.02 | 0.94 | 0.15 |

### 2.2 Experiment

The material used in this study was JIS SCM440 Cr–Mo low-alloy steel. The chemical composition is shown in Table 1. The mechanical properties after the heat treatments are shown in Table 2. The microstructure was tempered martensite with BCC lattice. The fracture toughness tests were carried out in accordance with the ASTM E 1820 standard. The $NH_3$ partial pressure was 1000 ppm and 10 000 ppm. The loading rate was $2.0 \times 10^{-3}$ and $2.0 \times 10^{-5}$ mm s$^{-1}$. The temperature was 293 K. A detailed description of the fracture toughness test system and compact tension (CT) specimen is provided in the SI-S3. The authors have used the same test system to investigate the impurity mitigation effect on HE.

## 3. Result and discussion

### 3.1 Theory

We optimize the lattice of BCC iron and obtain a lattice constant of 2.82 Å, which agrees with previous reports in the literature.[30] The surface optimization yields a slightly shorter distance between the first and second layers and a slightly longer distance between the second and third layers. First, we investigate the surface geometry and surface coverage by $NH_3$ molecules. The Fe(110) surface provides three distinct adsorption positions for $NH_3$ molecules. Those positions include the top, bridge, and hollow sites. All initial geometries in the process of geometry optimization converge to top site of the Fe(110) surface as shown in Fig. 1. We used different quantities of $NH_3$ molecules to cover the Fe surface, representing different coverage as shown in Fig. 2. We examined the adsorption energy of $NH_3$ on Fe(110) to determine the effect of different surface coverages and it is summarized in Table 3. The adsorption energy of $NH_3$ on the Fe(110) surface decreases with the increase of $NH_3$ coverage. This phenomenon is based on two reasons: (1) the pre-adsorbed $NH_3$ withdrew and localized electron density of the Fe surface, thus the electron density of the adjacent sites is no longer sufficient for the additional $NH_3$ adsorption; (2) the repulsive interactions between the $NH_3$ molecules. The most stable surface geometry is $NH_3$ molecules occupying top sites with coverage in the range of 11–33%.

To fully understand the effect of $NH_3$ on HE we investigated the decomposition of $NH_3$ with a relatively low $NH_3$ coverage (11%) on Fe(110) surface as shown in Fig. 3 This $NH_3$ decomposition process consists of three distinct steps. During each

Table 2 Mechanical properties of SCM440

| 0.2% proof strength (MPa) | Ultimate tensile strength (MPa) | Elongation | Reduction of area | Vickers hardness |
|---|---|---|---|---|
| 841 | 971 | 20% | 54% | HV329 |

Open Access Article. Published on 28 lokakuuta 2025. Downloaded on 26.3.2026 20.36.49.
This article is licensed under a Creative Commons Attribution-NonCommercial 3.0 Unported Licence.

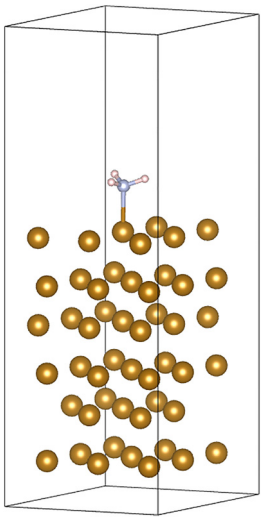

Fig. 1 Optimized geometry of $NH_3$ molecule adsorption geometry.

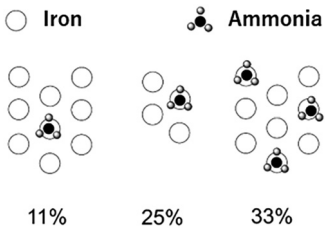


Fig. 2 Schematic presentation of ammonia coverage on Fe 110 surface.

step, $NH_3$, $NH_2$, and NH will release a hydrogen atom on the iron surface. The products of the $NH_3$ and hydrogen decomposition occupied different sites on the surface and consequently affected the surface coverage as shown in Table 4. When gas molecules interact with surfaces, they establish equilibrium with the surface products which is governed by the adsorption law, the reaction kinetics, and the partial pressure of the gas components. An increase in the gas partial pressure leads to an increase in the coverage of the adsorption products on the solid surface at a constant temperature.[31–33] Therefore, to understand the effect of $NH_3$ partial pressure, a higher $NH_3$ coverage (25%) on the Fe(110) surface as shown in Fig. 4 ($NH_3$ decomposition on the iron surface at elevated coverage) was investigated. The summary of the activation energy barriers ($E_a$) of $NH_3$ decomposition in each step (initial geometry, transition geometry, and end geometry) is shown in Table 5. The $E_a$ for the decomposition of $NH_3$ on the Fe(110) surface at 25% coverage is compared with that at 11% coverage. The first step of ammonia decomposition catalyzed by the Fe surface is affected by an increase in the surface coverage of ammonia. Additionally, as ammonia molecules only interact with individual Fe atoms, the Fe surface provides sufficient electrons to catalyze the decomposition of ammonia. Consequently, the $E_a$ for the first step decreases with increased $NH_3$ coverage. However, as $NH_3$ decomposes into $NH_2$ and NH, $NH_2$ and NH interact with two and three Fe atoms, respectively. This leads to the withdrawal and localization of more electrons, thereby reducing the available free electrons for catalysis. Therefore, both the second step ($NH_2 \rightarrow NH + H$) and the third step ($NH \rightarrow N + H$) of $NH_3$ decomposition exhibit significant changes with increased $NH_3$ coverage. The activation energy for the second decomposition step at 25% $NH_3$ coverage nearly doubles compared to that at 11% $NH_3$ coverage. Additionally, the reaction for the third decomposition step undergoes a transformation from an exothermic to an endothermic process as $NH_3$ coverage increases. Consequently, the higher $NH_3$ surface coverage mitigated $NH_3$ decomposition better.

We further investigate the $H_2$ dissociation process on the pure Fe(110) surface and Fe(110) surfaces pre-treated by $NH_3$ with different coverage. The geometries are summarized in Fig. 5. The activation energy barrier and dissociation energy of $H_2$ on the Fe(110) surface is shown in Table 6. Without $NH_3$ pre-adsorbed on the Fe(110) surface, the $H_2$ spontaneously dissociates on Fe(110) surface without an activation barrier. The dissociation energy of $H_2$ is −1.56 eV. At 11% coverage, the activation energy barrier for $H_2$ dissociation on Fe(110) surface is 0.04 eV, and the dissociation energy of $H_2$ is −1.54 eV. The dissociation energy slightly increased from 0.00 eV to 0.04 eV, which indicates that even at low coverage $NH_3$ can hinder $H_2$ dissociation. With the increase of $NH_3$ coverage on the Fe(110) surface from 11% to 33%, the activation barrier of $H_2$ dissociation increased up to 0.7 eV and the dissociation energy of $H_2$ decreased to −1.17 eV. The activation energy barrier would reduce the $H_2$ dissociation reaction rate. Decreasing the dissociation energy of $H_2$ would lead to easier $H_2$ molecule desorption. As a result, an increased activation energy barrier and decreased dissociation energy would lead to a decrease in the hydrogen atom concentration on the surface, thus, reducing the probability for hydrogen to permeate to Fe.

Chemical equilibrium is established by the mass fluxes between the gas phase and the surface equalize.[34] For molecules in contact with a solid surface at a fixed temperature, the Langmuir isotherm,[35] describes the partitioning between the gas phase and adsorbed species as a function of applied pressure. The basic assumption of this theory is: (1) assume the surface is homogeneous (no corrugations); (2) all sites are energetically equivalent, and the energy of adsorption is equal for all sites; (3) the gas adsorbs into an immobile state; (4) mono-layer coverage only; (5) no interactions between

Table 3 Adsorption energy of $NH_3$ on Fe 110 surface for different coverage

| Coverage | 11% $NH_3$ adsorbed on Fe(110) | 25% $NH_3$ adsorbed on Fe(110) | 33% $NH_3$ adsorbed on Fe(110) |
|---|---|---|---|
| Adsorption energy (eV) | −1.01 | −0.94 | −0.93 |

 This journal is © the Owner Societies 2025

Open Access Article. Published on 28 lokakuuta 2025. Downloaded on 26.3.2026 20.36.49.
This article is licensed under a Creative Commons Attribution-NonCommercial 3.0 Unported Licence.

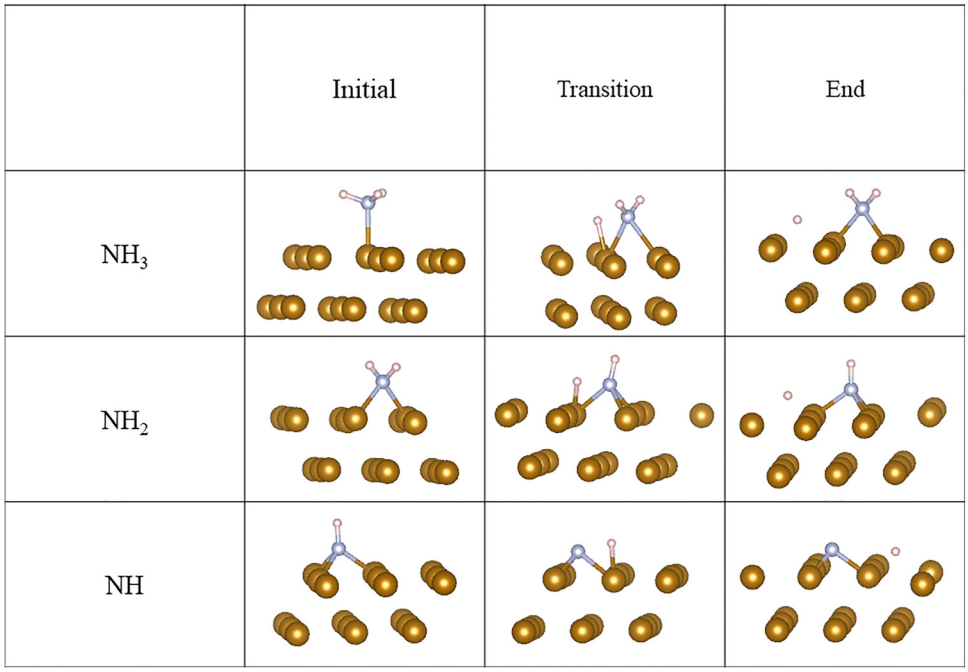


Fig. 3 $NH_3$-derived hydrogen atom on Fe(110) surface (11%).

Table 4 Occupied site of different adsorbed species on Fe(110) surface

| Adsorbed species | Occupied site |
|---|---|
| $NH_3$ | Top |
| $NH_2$ | Bridge |
| H atom derived by $NH_3$ | Bridge |
| NH | Hollow |
| H atom derived by $NH_2$ | Bridge |
| N | Hollow |
| H atom derived by NH | Bridge |

adsorbate molecules on adjacent sites.[36,37] The Langmuir theory consisted of different adsorption models: adsorption, competitive adsorption, dissociative adsorption, and competitive and dissociative adsorption. In this study, we investigate the competitive and dissociative adsorption of $NH_3$ and $H_2$ on the Fe(110) surface. Because $NH_3$–$H_2$ co-adsorption shows coverage effects, we benchmarked our conclusions against an interaction-inclusive isotherm following Christensen *et al.*;[38] details and sensitivity results are in SI-S1.

For the single adsorbate case, the model assumes adsorption and desorption as being elementary processes, where the rate of adsorption $r_{ad}$ and the rate of desorption $r_d$ are given by

$$r_{ad} = k_{ad} p_A [S] \tag{2}$$

$$r_d = k_d [A_{ad}] \tag{3}$$

where $p_A$ is the partial pressure of A over the surface, [S] is the surface concentration of the free site, $[A_{ad}]$ is the surface concentration of adsorbed specie A, and the $k_{ad}$ and $k_d$ are the constants of forward adsorption reaction, and backward desorption reaction in the above reaction.

At equilibrium, the rate of adsorption is equal to the rate of desorption. Setting $r_{ad} = r_d$, thus, the equilibrium constant

$$K_{eq}^{A} = \frac{[A_{ad}]}{p_A [s]} = \frac{k_{ad}}{k_d} \tag{4}$$

In eqn (4), the rate is given by the Arrhenius equation.[39] The equilibrium constant is independent of the pressure of the system or of the concentration of the reacting species. If the entire surface is covered by adsorbed species A and free sites, and we apply eqn (4) we can derive the Langmuir adsorption isotherm,

$$\theta_A = \frac{P_A K_A}{1 + P_A K_A} \tag{5}$$

For competitive adsorption, the surface is covered by A, B, and free sites, therefore, the expressions for adsorbed species of A and B in surface coverage $\theta_A$ and $\theta_B$ are as follows:

$$\theta_A = \frac{P_A K_A}{1 + P_A K_A + P_B K_B} \tag{6}$$

$$\theta_B = \frac{P_B K_B}{1 + P_A K_A + P_B K_B} \tag{7}$$

However, in the case of dissociation adsorption, the 1/2 power on $p_{D_2}$ arises because one gas phase molecule produces two adsorbed species.

In this study, we have performed surface coverage estimation based on the Langmuir theory. The Langmuir model neglects explicit adsorbate–adsorbate interactions and spatial correlations; such effects can matter when co-adsorbates interact or when pair-site requirements apply, and more detailed

Open Access Article. Published on 28 lokakuuta 2025. Downloaded on 26.3.2026 20.36.49.
This article is licensed under a Creative Commons Attribution-NonCommercial 3.0 Unported Licence.

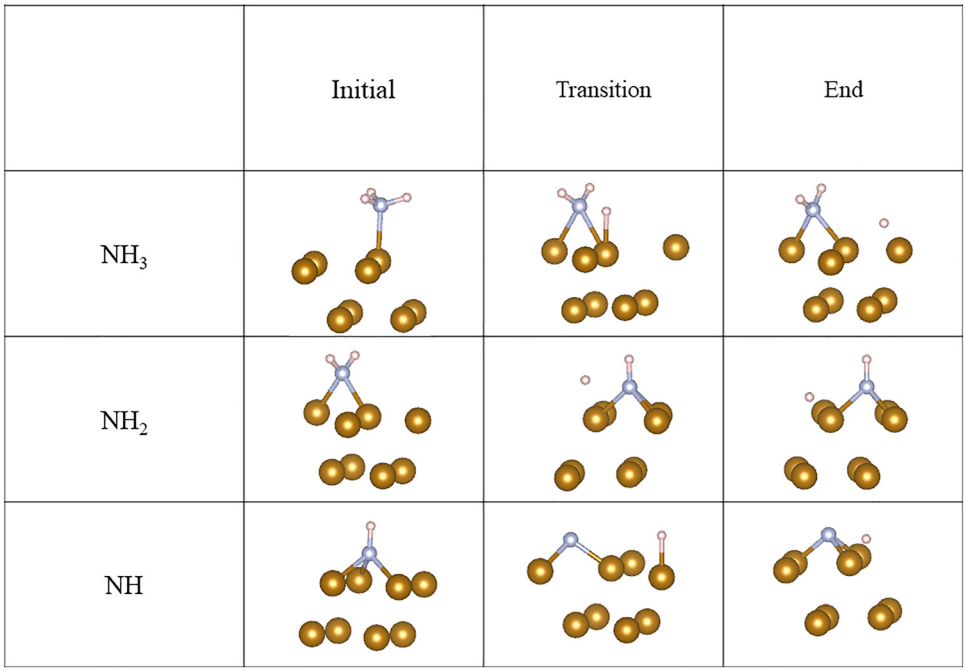


Fig. 4 $NH_3$-derived hydrogen atom on Fe(110) surface (25%).

Table 5 Decomposition and desorption $E_a$ of $NH_3$ on Fe(110) surface

| | Decomposition activation barrier (11%) | Decomposition activation barrier (25%) | Desorption activation barrier (11%) | Desorption activation barrier (25%) |
|---|---|---|---|---|
| $NH_3 \rightarrow NH_2 + H$ | 0.72 eV (Exo) | 0.68 eV (Exo) | 1.43 eV (Endo) | 1.39 eV (Endo) |
| $NH_2 \rightarrow NH + H$ | 0.45 eV (Exo) | 0.84 eV (Exo) | 1.36 eV (Endo) | 1.70 eV (Endo) |
| $NH \rightarrow N + H$ | 0.99 eV (Exo) | 1.05 eV (Endo) | 1.18 eV (Endo) | 0.98 eV (Exo) |

Exo = exothermic reaction. Endo = endothermic reaction.

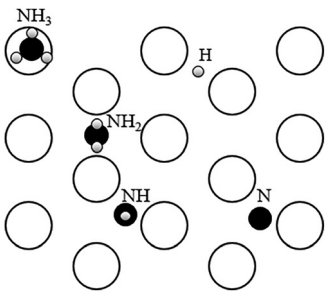


Fig. 5 Schematic presentation of adsorbate position on Fe 110 surface.

treatments (Fowler–Guggenheim/Temkin, cluster/Monte-Carlo or pair-site LH variants) may be used when needed. Here our objective is to rationalize relative trends; under these conditions, mean-field microkinetics remains a standard and defensible baseline. The $H_2$ molecule dissociates into two H atoms and can be solved by the 1/2 power on $p_{H_2}$. The complete $NH_3$ decomposition on the Fe surface is into an N atom and three H atoms. The kinetic derivation of $NH_3$ complete decomposition on the Fe surface, and complete $NH_3$ decomposition competitive with $H_2$ dissociation on the Fe surface are studied after considering $NH_3$ adsorbed on Fe(110) surface as a single molecule.

### 3.2 $NH_3$ mitigation effect on HE

To investigate the mechanism of $NH_3$ mitigation effect on HE, we first considered the $NH_3$ adsorbed on the Fe surface as a

Table 6 Dissociation energy of $H_2$

| Coverage | 0% $NH_3$ pre-adsorb Fe(110) | 11% $NH_3$ pre-adsorb Fe(110) | 25% $NH_3$ pre-adsorb Fe(110) | 33% $NH_3$ pre-adsorb Fe(110) |
|---|---|---|---|---|
| Activation energy (eV) | 0.00 | 0.04 | 0.06 | 0.07 |
| Dissociation energy (eV) | −1.56 | −1.54 | −1.22 | −1.17 |

Open Access Article. Published on 28 lokakuuta 2025. Downloaded on 26.3.2026 20.36.49.
This article is licensed under a Creative Commons Attribution-NonCommercial 3.0 Unported Licence.

molecule (without decomposition) and performed the Langmuir adsorption model, which assumes the adsorbate behaves as an ideal gas under isothermal conditions.[39–41] We apply the Langmuir competitive adsorption model in eqn (6) and (7), and further extend it to competitive and dissociative model due to $H_2$ is dissociative adsorption on the Fe surface. The 1/2 power on $H_2$ arises because hydrogen atoms occupy two sites on the surface. We used the data in Tables 5 and 6 to modify the Langmuir competitive adsorption model for the $NH_3$ and $H_2$ competitive and dissociative co-adsorption on the Fe(110) surface. The surface coverage equation for $NH_3$ adsorption and $H_2$ dissociative adsorption is given below (eqn (8) and (9), respectively). In those equations, $\theta_{NH_3}$ and $\theta_H$ are denoted by the fractional occupancy on the surface by $NH_3$ or atomic hydrogen, respectively. The activation barriers for different $NH_3$ coverage are taken from the DFT calculations, the temperature is set to 293 K, and high-purity $H_2$ was considered with 1000 ppm and 10 000 ppm partial pressure of $NH_3$ to match the experiment conditions. We used two different coverage models to represent the different $NH_3$ partial pressure on $H_2$ gas because increased partial pressure leads to higher surface coverage.[42,43] Thus, 1 $NH_3$ on the 9 surface Fe model represents the lower partial pressure of $NH_3$ in $H_2$, and 1 $NH_3$ on the 4 surface Fe model represents the higher partial pressure of $NH_3$ in $H_2$.

$$\theta_{NH_3} = \frac{P_{NH_3}K_{NH_3}}{1 + P_{NH_3}K_{NH_3} + \sqrt{P_{H_2}K_{H_2}}} \tag{8}$$

$$\theta_H = \frac{\sqrt{P_{H_2}K_{H_2}}}{1 + P_{NH_3}K_{NH_3} + \sqrt{P_{H_2}K_{H_2}}} \tag{9}$$

In eqn (8) and (9) $K_{NH_3}$ and $K_{H_2}$ denote the $NH_3$ and $H_2$ adsorption/desorption equilibrium constants for activation barriers listed in Tables 5 and 6, which were calculated by DFT. $P_{NH_3}$ and $P_{H_2}$ denote the partial pressure of $NH_3$ and $H_2$, respectively. The rate constants were estimated using the Arrhenius equation, where $A$ is a preexponential factor, $R$ is the gas constant, $T$ is the temperature, and $E_a$ is the activation barrier. The equilibrium constants are computed as the ratio between the adsorption and the desorption rate constants. The preexponential factor is computed as the reaction attempt frequency which is given by the product of the vibration frequencies at the resting site divided by the product of vibration frequencies in the transition state (the single imaginary frequency is excluded). It is important to note that the pre-exponential factor differs for the forward and reversed reactions. While the vibration frequencies at transition state are the same, they differ for the starting and end point of the reaction (product and reactant). The vibration frequencies are obtained through Hessian deionization in the DFT calculations.

From the cooperative adsorption/desorption/dissociation model in eqn (8) and (9), we calculated the $NH_3$ and atomic hydrogen coverage on the Fe surface with different $NH_3$ partial pressure, the result is shown in Table 7. The hydrogen atom coverage on the Fe(110) surface is decreasing with the increase in $NH_3$ coverage, which is achieved by increased $NH_3$ partial pressure. There is no direct study related to the ratio of atomistic hydrogen surface coverage on iron surface and initiation of crack growth induced by HE. We have reported that hydrogen atom coverage on the iron surface is 0.6% with CO 75% coverage.[16] Experimental results show that CO could mitigate the HE.[16] For $NH_3$ 25% coverage on Fe(110) surface the atomic hydrogen coverage is 0.01%, which is below 0.60%. Thus, we can expect that $NH_3$ could possibly mitigate HE if it could have a faster adsorption rate compared to $H_2$.

Table 7 Coverage of $NH_3$ and atomic hydrogen on Fe(110) surface non-dissociative $NH_3$

| Condition | $H_2$ + 1000 ppm $NH_3$ | $H_2$ + 10 000 ppm $NH_3$ |
|---|---|---|
| $\theta_{NH_3}$ | 10% | 25% |
| $\theta_H$ | 1.70% | 0.01% |

Surface reactions can be classified into two generic types. The first includes reactions between two adsorbed species or between an adsorbed species and a vacant site (Langmuir–Hinshelwood process), which is fitting for our consideration of coadsorption between $NH_3$ and $H_2$. The other reaction is called the Eley–Rideal process, which is considering that adsorbed species form a product.

Based on the Langmuir–Hinshelwood process, for randomly distributed adsorbates on a surface in the absence of adsorbate-adsorbate interactions, the rate of reaction is given by eqn (10).

$$r_r = k\theta_A\theta_v \tag{10}$$

$$k = Ae^{-\frac{E_a}{RT}} \tag{11}$$

where $\theta_A$ is the surface coverage of species A, and $\theta_v$ is the fraction of the vacant sites. We calculated the pre-exponential factor (frequency factor) of $NH_3$ and $H_2$ using DFT frequency calculations (see eqn (1)) for calculating their reaction rate coefficient (eqn (11)). Table 8 shows the pre-exponential factors, reaction rate coefficient, and reaction rate of $NH_3$ and $H_2$ on the Fe(110) surface. The reaction rate coefficient of $NH_3$ and $H_2$ on the Fe(110) surface is based on eqn (10). We use the computed pre-exponential factors and activation energies for $NH_3$ and hydrogen from Table 8 to estimate the equilibrium constants for $NH_3$ and hydrogen adsorption/desorption on Fe(110) surface. Then, we use those equilibrium constants in eqn (10) and (11) with the $NH_3$ partial pressure for 1000 ppm and 10 000 ppm to estimate the hydrogen and $NH_3$ reaction rates in Table 8.

Table 8 Pre-exponential factor, reaction rate coefficient, and reaction rate of $NH_3$ and $H_2$

| | $NH_3$ | $H_2$ |
|---|---|---|
| $A$ (Hz) | $3.18 \times 10^{20}$ | $3.90 \times 10^{11}$ |
| $k$ ($s^{-1}$) | $3.14 \times 10^{20}$ | $3.92 \times 10^{11}$ |
| $r_{r(11\%NH_3)}$ ($s^{-1}$) | $2.77 \times 10^{19}$ | $5.85 \times 10^{9}$ |
| $r_{r(25\%NH_3)}$ ($s^{-1}$) | $5.88 \times 10^{19}$ | $2.92 \times 10^{7}$ |

Open Access Article. Published on 28 lokakuuta 2025. Downloaded on 26.3.2026 20.36.49.
This article is licensed under a Creative Commons Attribution-NonCommercial 3.0 Unported Licence.

With increasing the coverage of $NH_3$ from 11% to 25%, the reaction rate of $H_2$ with the Fe(110) surface decreases from $5.85 \times 10^9$ $s^{-1}$ to $2.92 \times 10^7$ $s^{-1}$. Thus, increasing $NH_3$ partial pressure reduces hydrogen dissociation rate on Fe(110) surface. On the other hand, the adsorption rate of $NH_3$ is significantly faster than $H_2$, which indicates that $NH_3$ preferentially adsorbs on the Fe(110) surface compared to $H_2$.

### 3.3 Effect of $NH_3$ decomposition on its mitigation effect on HE (while competing with $H_2$ dissociation)

To fully understand the effect of $NH_3$ competing with $H_2$ with respect to HE, we divided the process of $NH_3$ decomposition into four steps, and simultaneously considered the dissociation of $H_2$. The decomposition mechanism of $NH_3$ includes the chemisorption of $NH_3$ on the catalyst surface,[40,43–46] stepwise dehydrogenation of $NH_3$ to $NH_2$ + H, NH + H, N + H. The adsorption of all the species follows the Langmuir isotherm model, therefore it is assumed that the surface sites are energetically equivalent, and each site can hold at most one adsorbed species. The mechanism can be described according to the following sequence of elementary reactions as shown in (R1)–(R4):

$$NH_3 + * \rightleftharpoons NH_3* \quad (R1)$$

$$NH_3* + * \rightleftharpoons NH_2* + H* \quad (R2)$$

$$NH_2* + * \rightleftharpoons NH* + H* \quad (R3)$$

$$NH* + * \rightleftharpoons N* + H* \quad (R4)$$

To establish the kinetic model of competitive and dissociative co-adsorption between $NH_3$ and $H_2$ on the Fe(110) surface we must consider the $H_2$ dissociation. The reaction of $H_2$ dissociation on the Fe(110) surface can be expressed by the chemical reaction (R5) below:

$$H_2 + 2* \rightleftharpoons 2H* \quad (R5)$$

The term * denotes a vacant site, and $NH_3$*, $NH_2$*, NH*, N*, and H* are the adsorbed species. $NH_3$ and $H_2$ represent the free gaseous state. If all the above reactions are equilibrium that the constants of equilibrium ($K_1$, $K_2$, $K_3$, $K_4$, and $K_5$) are given by eqn (3) for each step. The reaction rate coefficient $k$ $\left(\overrightarrow{k_1}, \overleftarrow{k_1}, \overrightarrow{k_2}, \overleftarrow{k_2}, \overrightarrow{k_3}, \overleftarrow{k_3}, \overrightarrow{k_4}, \overleftarrow{k_4}\right)$ in each step is given by Arrhenius equation (eqn (11)).

Then, we investigate the hydrogen atom surface coverage from the $NH_3$ decomposition on the Fe(110) surface step by step and compare the competing $H_2$ dissociation reaction. We assume that the reaction stops at each step and reaches equilibrium. Therefore, the whole process is divided into three cases denoted with 1, 2, and 3.

In order to keep the main text concise, we only summarize the setup of the staged $NH_3$ decomposition while competing with $H_2$ dissociation. We analyze three quasi-equilibrated stopping cases—Case 1 ($NH_3* \rightleftharpoons NH_2* + H*$), Case 2 (up to NH* + H*), and Case 3 (up to N* + H*)—with competitive dissociative $H_2$ adsorption ($H_2 + 2* \rightleftharpoons 2H*$). The corresponding equilibrium relations ($K_1$–$K_5$), Arrhenius parameterization, and the site balance are solved self-consistently at 293 K under the stated gas compositions. The full mass-balance equations, algebraic solution, and numerical procedure are provided in SI-S2, and the resulting coverages are reported in Table 9.

The hydrogen coverage of each case is summarized in Table 9. From Case 1 to Case 3, owing to the $NH_3$ decomposition, the hydrogen atom coverage on Fe(110) surface significantly increased from 2.96% to 8.42% (1000 vppm $NH_3$), 4.73% to 15.20% (10 000 vppm $NH_3$). The hydrogen atom coverage on Fe(110) surface increased with the $NH_3$ decomposition and the $NH_3$ partial pressure. The final step of $NH_3$ decomposition to N and H has almost no contribution to H atom coverage on the Fe surface. However, the HE mitigation effect is not only affected by coverage, but also time dependent through the reaction rate. Therefore, we investigate the decomposition rate of $NH_3$ at each step.

We use the Arrhenius equation (eqn (11)) where the pre-exponential factor $A$ is taken from Table 8, the $E_a$ is taken from Table 5, $R$ is the universal gas constant, and $T$ is 293 K for fitting with the fracture toughness test condition. The reaction rate coefficient of $NH_3$ decomposition in each step can be calculated as shown in Table 10. Under the same $NH_3$ partial pressure, the reaction rate coefficient of $NH_3$, $NH_2$, and NH is decreasing. For lower $NH_3$ partial pressure (1000 vppm) we find a reduction in the reaction rate coefficient from $NH_2$ to NH, which demonstrates that the last step of $NH_3$ decomposition (NH → N + H) is the slowest step. However, the first two decomposition steps ($NH_3 \rightarrow NH_2 + H$; $NH_2 \rightarrow NH + H$) are characterized with high reaction rate coefficients. When the $NH_3$ partial pressure is increased to 10 000 vppm we find a reduction in the reaction rate coefficient from $NH_3$ to $NH_2$, which indicates that the $NH_3$ decomposition is not likely to occur on the experimental time scale. Thus, during the experimental time scale, increased $NH_3$ partial pressure will decrease the $NH_3$ decomposition rate

Table 9 Summary of hydrogen coverage on Fe(110) surface

| | H coverage 1000 vppm $NH_3 + H_2$ | H coverage 10 000 vppm $NH_3 + H_2$ |
|---|---|---|
| Case 1 | 2.96% | 4.37% |
| Case 2 | 8.42% | 15.20% |
| Case 3 | 8.42% | 15.20% |

Table 10 Reaction rate coefficient $k$ of $NH_3$ decomposition

| | $NH_3$ | $NH_2$ | NH |
|---|---|---|---|
| $k$ (1000 vppm $NH_3$) ($s^{-1}$) | $1.368 \times 10^8$ | $7.284 \times 10^5$ | $2.130 \times 10^{-1}$ |
| $k$ (10 000 vppm $NH_3$) ($s^{-1}$) | $6.656 \times 10^8$ | $1.459 \times 10^{-1}$ | $1.986 \times 10^{-2}$ |

Open Access Article. Published on 28 lokakuuta 2025. Downloaded on 26.3.2026 20.36.49.
This article is licensed under a Creative Commons Attribution-NonCommercial 3.0 Unported Licence.

constant, and in a limited time scale, before the equilibrium is reached, it might successfully kinetically mitigate HE.

Our theoretical results at equilibrium show that the hydrogen coverage on Fe(110) surface increases with the increase in $NH_3$ partial pressure. However, the $NH_3$ reaction kinetics suggests that at short time intervals $NH_3$ will decompose to $NH_2$, NH and H at low partial pressure (1000 vppm) and only to $NH_2$ and H at high partial pressure (10 000 vppm). Thus, the H surface coverage will be kinetically locked to 8.42% at 1000 vppm $NH_3$ partial pressure and 4.37% at 10 000 vppm $NH_3$ partial pressure. As a result, increasing the $NH_3$ partial pressure would have a mitigating effect on HE.

## 4. Fracture toughness test results

Hydrogen embrittlement is a phenomenon that includes a series of processes: surface adsorption/desorption, molecular dissociation, surface/sub-surface migration, hydrogen dissolution, defects trapping, grain boundaries segregation, hydrogen concentration ahead of the crack tip, *etc.* In this study, we designed an experiment where we kept all conditions the same and attempted to only relate the crack growth resistance ability of the material to the ammonia partial pressure and loading rate.

The fracture toughness test results, shown in Fig. 6, illustrate the relationship between the *J*-integral value and crack extension ($\Delta a$). The fracture toughness of the material, determined by the *J*-integral value at the intersection of the $J$–$\Delta a$ curve and the 0.2 mm offset line, is evaluated in accordance with the ASTM E1820 standard. This value represents the material's resistance to the onset of crack extension. The data obtained in high-purity $N_2$ serves as the reference.

At the loading rate was $2.0 \times 10^{-3}$ mm s$^{-1}$, there was a reduction of fracture toughness of material in $H_2$ gas. This result indicates that hydrogen embrittlement occurred. However, when 1000 ppm $NH_3$ is added to $H_2$ gas, the reduction is recovered. It was confirmed that $NH_3$ has a mitigating effect on hydrogen embrittlement. The $NH_3$ mitigation effect increased with increased $NH_3$ partial pressure.

Additionally, we conducted fracture toughness tests in nitrogen gas with added $NH_3$. If $NH_3$ has neither a detrimental nor an improving effect, it is expected that the $J$–$\Delta a$ curve would match that obtained in pure $N_2$. During the fracture toughness test with 1000 ppm $NH_3$ at a loading rate of $2.0 \times 10^{-3}$ mm s$^{-1}$, no reduction in fracture toughness was observed. However, surprisingly, when the loading rate was reduced to 1/100 (*i.e.*, $2.0 \times 10^{-5}$ mm s$^{-1}$), the $J$–$\Delta a$ curve for nitrogen gas with 1000 ppm $NH_3$ shifted significantly downward, resulting in a marked decrease in fracture toughness.

As shown in Fig. 7, the fracture surface obtained in nitrogen gas with 1000 ppm $NH_3$ exhibited a quasi-cleavage fracture morphology, resembling the fracture surface obtained in the fracture toughness test in hydrogen. This observation suggests that hydrogen embrittlement occurred despite the absence of $H_2$ gas in the test environment. A possible mechanism is the production of hydrogen atoms due to the decomposition of $NH_3$ on the iron surface, facilitated by the catalytic action of the Fe surface (Fig. 8).

In summary, $NH_3$ exhibits both mitigating and inducing effects on hydrogen embrittlement, depending on the loading rate. If this assumption is correct, the loading rate dependence of $NH_3$'s mitigating effect in $H_2$ + $NH_3$ environments can be clearly explained. As shown in Fig. 7, the addition of 1000 ppm $NH_3$ significantly mitigated HE at a loading rate of $2 \times 10^{-3}$ mm s$^{-1}$. However, this mitigating effect drastically diminished when the loading rate was reduced to $2 \times 10^{-5}$ mm s$^{-1}$.

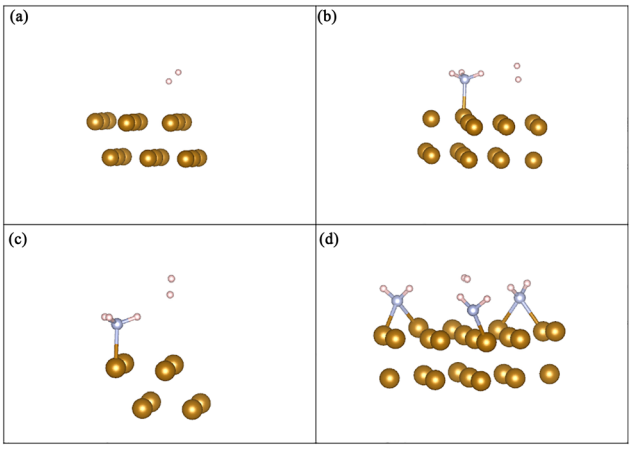


Fig. 6 Molecular hydrogen dissociation on the Fe(110) surface with (a) 0%, (b) 11%, (c) 25%, and (d) 33% $NH_3$ coverage.

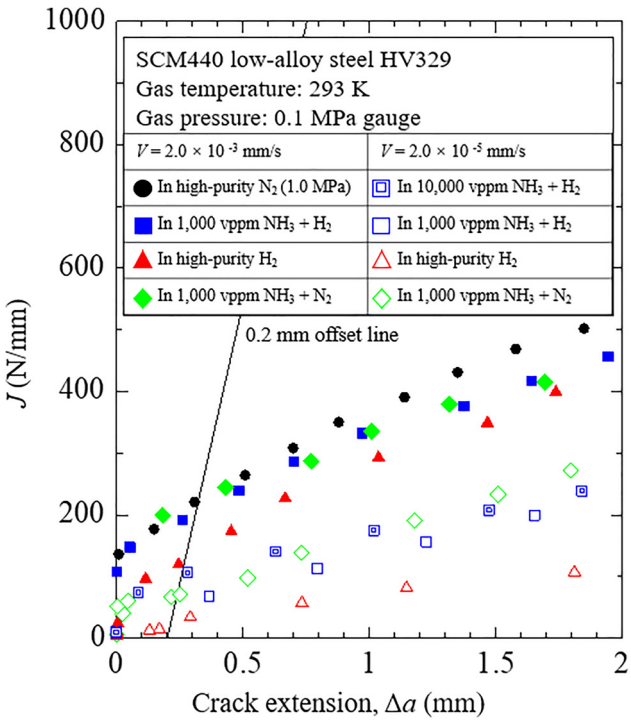


Fig. 7 Mitigation effect of $NH_3$ on HE and its loading rate and concentration dependency.

Open Access Article. Published on 28 lokakuuta 2025. Downloaded on 26.3.2026 20.36.49.
This article is licensed under a Creative Commons Attribution-NonCommercial 3.0 Unported Licence.

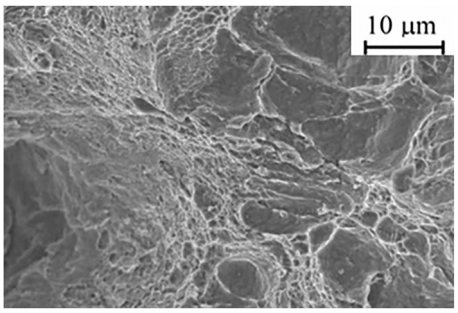


Fig. 8 Fracture surface tested in 1000 ppm $NH_3$ + $N_2$.

According to the DFT simulation results shown in Table 8 and 10, the adsorption rate of $NH_3$ on the Fe surface is significantly higher than its decomposition rate. Therefore, at a relatively high loading rate, crack propagation occurs while the Fe surface is predominantly covered by $NH_3$ molecules, suppressing hydrogen uptake into the material. In contrast, at a sufficiently low loading rate, the slower crack propagation allows $NH_3$ to decompose into H and $NH_2$. The hydrogen produced from $NH_3$ decomposition then becomes a source of hydrogen embrittlement, negating the mitigating effect of $NH_3$.

However, Fig. 7 still presents a puzzling result. Specifically, in the fracture toughness test conducted at a loading rate of $2.0 \times 10^{-5}$ mm $s^{-1}$, the fracture toughness in the 10 000 ppm $NH_3$ + $H_2$ environment was higher than that in the 1000 ppm $NH_3$ + $H_2$ environment. If the previous discussion—that $NH_3$ decomposition produces hydrogen atoms at relatively low loading rates—is correct, it would be expected that increasing the $NH_3$ concentration would further reduce fracture toughness due to an increase in hydrogen atom production. However, the observed result is the opposite.

This anomaly can be explained by the results of the DFT calculations shown in Table 10. As shown in the figure, the $NH_3$ decomposition rate ($NH_2 \rightarrow NH + H$) dramatically decreases with increasing $NH_3$ partial pressure. This is because $NH_3$ decomposition requires a vacant site adjacent to the adsorbed $NH_3$ on the Fe surface. An increase in $NH_3$ concentration leads to higher surface coverage of $NH_3$ on the Fe surface, thereby reducing the availability of vacant sites. Consequently, the adsorbed $NH_3$ loses the opportunity to decompose as the $NH_3$ concentration increases.

## 5. Conclusion

$NH_3$ was preferentially adsorbed on the Fe(110) surface because the adsorption rate of $NH_3$ on the Fe(110) surface is significantly higher than $H_2$. When the coverage of $NH_3$ on the Fe(110) surface was 25%, the atomic hydrogen coverage on Fe(110) surface would be 0.01%. In conclusion, preferentially adsorbed $NH_3$ mitigates the HE in gaseous hydrogen by hindering hydrogen uptake. The $NH_3$ decomposition reaction has a strong time dependence because the adsorption rate of $NH_3$ is much higher than its decomposition rate. Therefore, $NH_3$ decomposition occurs only when reaction time is sufficient. The $NH_3$ decomposition rate ($NH_2 \rightarrow NH + H$) decreased as $NH_3$ partial pressure increased resulting in hindering $NH_3$-derived hydrogen supply. As a result, insufficient time for $NH_3$ further decomposition leads to lower H atom coverage on the Fe surface even at high $NH_3$ partial pressures. Therefore, increased $NH_3$ partial pressure could successfully mitigate HE through a kinetic mechanism. Our fracture toughness test results supported the theoretical results well. The test duration was controlled by the loading rate. Under the relatively higher loading rate, $NH_3$ mitigates HE. However, as we reduced the loading rate, the $NH_3$ mitigation effect on HE decreased due to its decomposition. Under the relatively slower loading rate, the $NH_3$ mitigation effect increased with increased $NH_3$ partial pressure. This kinetic modeling highlights two practical control parameters for hydrogen entry: $NH_3$ surface coverage (*via* partial pressure) and exposure time scale (loading rate). At high coverage and short times, rapid $NH_3$ adsorption suppresses $H_2$ dissociation; over longer times, slow $NH_3$ decomposition can supply H to the surface. These findings suggest pressure–time operating windows to limit hydrogen ingress and offer a transferable protocol for HE mitigation strategy.

## Conflicts of interest

There are no conflicts to declare.

## Data availability

The manuscript contains the computed results and detailed explanation how the simulations can be repeated and verified. In addition, supplementary information (SI) file is provided containing description of the experimental setup. In case further information is needed, it can be obtained *via* email from the corresponding author. Supplementary information is available. See DOI: **https://doi.org/10.1039/d5cp02423d**.

## Acknowledgements

This study was supported by JST SPRING, Grant Number JPMJSP2136. This study was supported by the World Premier International Research Center Initiative (WPI), MEXT, Japan. The International Institute for Carbon-Neutral Energy Research (WPI-I2CNER) is supported by the World Premier International Research Center Initiative (WPI), MEXT, Japan. Kyushu University platform of Inter-transdisciplinary Energy Research (Q-PIT), Japan.

## References

1 D. Hardie and P. McIntyre, The low-temperature embrittlement of niobium and vanadium by both dissolved and precipitated hydrogen, *Metall. Trans. A*, 1973, **4**, 1247–1254.
2 A. R. Troiano, The role of hydrogen and other interstitials in the mechanical behavior of metals, *Trans. Am. Soc. Met.*, 1960, **52**, 54–80.

Open Access Article. Published on 28 lokakuuta 2025. Downloaded on 26.3.2026 20.36.49.
This article is licensed under a Creative Commons Attribution-NonCommercial 3.0 Unported Licence.

3 H. K. Birnbaum and P. Sofronis, Hydrogen-enhanced localized plasticity—a mechanism for hydrogen-related fracture, *Mater. Sci. Eng., A*, 1994, **176**, 191–202.
4 C. D. Beachem, A new model for hydrogen-assisted cracking (hydrogen ''embrittlement''), *Metall. Trans.*, 1972, **3**, 441–455.
5 S. Suresh and R. O. Ritchie, Mechanistic dissimilarities between environmentally influenced fatigue-crack propagation at near-threshold and higher growth rates in lower strength steels, *Mater. Sci.*, 1982, **16**, 529–538.
6 D. Hardie and S. Liu, The effect of stress concentration on hydrogen embrittlement of a low alloy steel, *Corros. Sci.*, 1996, **38**, 721–733.
7 H. E. Townsend, Effects of zinc coatings on the stress corrosion cracking and hydrogen embrittlement of low-alloy steel, *Metall. Mater. Trans. A*, 1975, **6**, 877–883.
8 P. S. Lam, R. L. Sindelar, A. J. Duncan and T. M. Adams, Literature Survey of Gaseous Hydrogen Effects on the Mechanical Properties of Carbon and Low Alloy Steels, *J. Press Vessel. Technol.*, 2009, **131**, 1–14.
9 R. P. Gangloff, Gaseous hydrogen embrittlement of high strength steels, *Metall. Mater. Trans. A*, 1977, **8**, 1043–1053.
10 B. P. Somerday, P. Sofronis and K. A. Nibur, *et al.*, Elucidating the variables affecting accelerated fatigue crack growth of steel in hydrogen gas with low oxygen concentrations, *Acta Mater.*, 2013, **61**, 6153–6170.
11 R. Komoda, K. Yamada and M. Kubota, *et al.*, The inhibitory effect of carbon monoxide contained in hydrogen gas environment on hydrogen-accelerated fatigue crack growth and its loading frequency dependency, *Int. J. Hydrogen Energy*, 2019, **44**, 29007–29016.
12 A. Staykov, J. Yamabe and B. P. Somerday, Effect of hydrogen gas impurities on the hydrogen dissociation on iron surface, *Int. J. Quantum Chem.*, 2014, **114**, 626–635.
13 A. Staykov, R. Komoda and M. Kubota, *et al.*, Coadsorption of CO and $H_2$ on an Iron Surface and Its Implication on the Hydrogen Embrittlement of Iron, *J. Phys. Chem. C*, 2019, **123**, 30265–30273.
14 R. Komoda, M. Kubota and S. Yoshida, *et al.*, Inhibition of Hydrogen Embrittlement of Cr-Mo Steel by the Addition of Impurities to Hydrogen Environment and the Effect of Material Strength. *Paper presented at the The 28th International Ocean and Polar Engineering Conference*, Sapporo, Japan, June 2018.
15 R. Komoda, M. Kubota and A. Staykov, *et al.*, Inhibitory effect of oxygen on hydrogen-induced fracture of A333 pipe steel, *FFEMS*, 2019, **42**, 1387–1401.
16 J. H. Holbrook, H. J. Cialone and E. W. Collings, *et al.*, Control of hydrogen embrittlement of metals by chemical inhibitors and coatings, in *Woodhead Publishing Series in Metals and Surface Engineering, Gaseous Hydrogen Embrittlement of Materials in Energy Technologies*, ed. R. P. Gangloff and B. P. Somerday, Woodhead Publishing, 2012, ch. 5, vol. 1, pp. 129–153.
17 A. Nagao, J. Koga, S. Takagi, H. Ono and N. Ishikawa, *Experimental and computational studies on hydrogen entry into steel exposed to high-pressure hydrogen gas*, ISIJ conference, Tokyo, Japan, 2018.
18 F. Bakhshi and N. Farhadian, Co-doped graphene sheets as a novel adsorbent for hydrogen storage: DFT and DFT-D3 correction dispersion study, *Int. J. Hydrogen Energy*, 2018, **43**, 8355–8364.
19 A. Staykov, J. Yamabe and B. P. Somerday, Effect of hydrogen gas impurities on the hydrogen dissociation on iron surface, *Int. J. Quantum Chem.*, 2014, **114**, 626–635.
20 B. P. Somerday, P. Sofronis and K. A. Nibur, *et al.*, Elucidating the variables affecting accelerated fatigue crack growth of steel in hydrogen gas with low oxygen concentrations, *Acta Mater.*, 2013, **61**, 6153–6170.
21 A. Staykov, R. Komoda and M. Kubota, *et al.*, Coadsorption of CO and $H_2$ on an Iron Surface and Its Implication on the Hydrogen Embrittlement of Iron, *J. Phys. Chem. C*, 2019, **123**, 30265–30273.
22 G. T. Gunasooriya, *et al.*, CO Adsorption on Pt(111): From Isolated Molecules to Ordered High-Coverage Structures, *ACS Catal.*, 2018, **8**, 10225–10233.
23 C. Samanta, Direct synthesis of hydrogen peroxide from hydrogen and oxygen: An overview of recent developments in the process, *Appl. Catal., A*, 2008, **350**, 133–149.
24 A. Manasilp and E. Gulari, Selective CO oxidation over Pt/alumina catalysts for fuel cell applications, *Appl. Catal., B*, 2002, **37**, 17–25.
25 V. Srikrishnan, Selective adsorption and hydrogen embrittlement, *Metall. Mater. Trans. A*, 1976, **11**, 1669–1675.
26 G. T. Gunasooriya, *et al.*, CO Adsorption on Pt(111): From Isolated Molecules to Ordered High-Coverage Structures, *ACS Catal.*, 2018, **8**, 10225–10233.
27 M. R. Louthan and R. E. Swanson, Material defects, gas purity and hydrogen embrittlement, *Int. J. Hydrogen Energy*, 1985, **10**, 551–554.
28 S. Smidstrup and T. Markussen, *et al.*, Quantum ATK: an integrated platform of electronic and atomic-scale modelling tools, *J. Phys. Condens.*, 2019, **32**, 1–36.
29 J. R. Chelikowsky and S. G. Louie, First-principles linear combination of atomic orbitals method for the cohesive and structural properties of solids: application to diamond, *Phys. Rev. B: Condens. Matter Mater. Phys.*, 1984, **29**, 6–15.
30 J. A. Yan, C. Y. Wang and S. Y. Wang, Generalized-stacking-fault energy and dislocation properties in bcc Fe: a first-principles study, *Phys. Rev. B: Condens. Matter Mater. Phys.*, 2000, **70**, 1–5.
31 G. M. Hermse and F. Frechard, *et al.*, Combining density-functional calculations with kinetic models: NO/Rh(111), *J. Chem. Phys.*, 2003, **118**, 7081–7089.
32 F. Mafuné, J. M. Bakker and S. Kudoh, Dissociative adsorption of NO introduces flexibility in gas phase $Rh^{6+}$ clusters leading to a rich isomeric distribution, *Chem. Phys. Lett.*, 2021, **780**, 138937.
33 M. H. John and T. Ziegler, Density Functional Theory and Kinetic Studies of Methanation on Iron Surface, *J. Phys. Chem. C*, 2007, **111**, 11012–11025.

Open Access Article. Published on 28 lokakuuta 2025. Downloaded on 26.3.2026 20.36.49.
This article is licensed under a Creative Commons Attribution-NonCommercial 3.0 Unported Licence.

34 M. W. Lindauer, The evolution of the concept of chemical equilibrium from 1775 to 1923, *J. Chem. Educ.*, 1962, **39**, 384–390.
35 I. Langmuir, The Adsorption of Gases on Plane Surface of Glass, Mica and Platinum, *J. Am. Chem. Soc.*, 1918, **40**, 1361–1402.
36 I. Langmuir, *"Part I" The Research Laboratory of the General Electric Company*, 1916, p. 2221.
37 I. Langmuir, *"Part II" The Research Laboratory of the General Electric Company*, 1918, p. 1848.
38 S. Hansen, An Adsorption Isotherm That Includes the Interactions Between Adsorbates, *J. Phys. Chem. C*, 2025, **129**, 5393–5407.
39 S. Arrhenius, Quantitative relationship between the rate a reaction proceed and its temperature, *J. Phys. Chem.*, 1889, **4**, 226–248.
40 A. Staykov, R. Komoda and M. Kubota, *et al.*, Coadsorption of CO and $H_2$ on an Iron Surface and Its Implication on the Hydrogen Embrittlement of Iron, *J. Phys. Chem. C*, 2019, **123**, 30265–30273.
41 A. Staykov, S. Fukumori and K. Yoshizawa, *et al.*, Interaction of SrO-terminated $SrTiO_3$ surface with oxygen, carbon dioxide, and water, *J. Mater. Chem. A*, 2018, **6**, 22662–22672.
42 G. Pekridis, K. Kalimeri and N. Kaklidis, *et al.*, Study of the reverse water gas shift (RWGS) reaction over Pt in a solid oxide fuel cell (SOFC) operating under open and closed-circuit conditions, *Catal. Today*, 2007, **127**, 337–346.
43 W. Tsai and W. H. Weinberg, Steady-State Decomposition of Ammonia on the Ru(001) Surface, *J. Phys. Chem.*, 1987, **91**, 5302–5307.
44 G. Ertl, Surface Science and Catalysis—Studies on the Mechanism of Ammonia Synthesis: The P. H. Emmett Award Address, *Chem. Rev.*, 1980, **21**, 201–223.
45 Z. Kowalczyk, J. Sentek, S. Jodzis, M. Muhler and O. Hinrichsen, Effect of Potassium on the Kinetics of Ammonia Synthesis and Decomposition over Fused Iron Catalyst at Atmospheric Pressure, *J. Catal.*, 1997, **167**, 407–414.
46 G. Centi and S. Perathoner, Adsorption and Reactivity of No on Copper-on-Alumina Catalysts: II. Adsorbed Species and Competitive Pathways in the Reaction of No with $NH_3$ and $O_2$, *J. Catal.*, 1995, **152**, 93–102.

 This journal is © the Owner Societies 2025